metals

MDPI

Article

Microstructural Evolution, HAZ Softening and Failure Behavior of Large-Diameter QT/AR 1045 Steel CDFW Joints

Shuwan Cui [1], Dao'ai Zhou [1], Zuojin Qin [2,*], Xingui Ma [1], Guiyou Zhou [1], Mingqian Gao [2] and Fuyuan Tian [2]

[1] School of Mechanical and Automotive Engineering, Guangxi University of Science and Technology, Liuzhou 545006, China; swcui@gxust.edu.cn (S.C.); 20240103077@stdmail.gxust.edu.cn (D.Z.); 20240102033@stdmail.gxust.edu.cn (X.M.); 20240103078@stdmail.gxust.edu.cn (G.Z.)

[2] Liugong Machinery Co., Ltd., Liuzhou 545006, China; yusheng418@163.com (M.G.); z145111705611@163.com (F.T.)

* Correspondence: a19207820524@163.com; Tel.: +86-192-0782-0524

Abstract

As piston rods for excavator boom hydraulic cylinders shift from integral forging to welded assemblies of separately manufactured rod bodies and rod heads, joint reliability becomes critical to load-bearing performance. In this study, 60 mm diameter quenched-and-tempered/as-rolled 1045 steel joints were fabricated by continuous-drive friction welding under three coupled secondary-friction pressure–time conditions. Joints made with two quenched-and-tempered base metals were compared under the same high-pressure/short-time condition. Optical microscopy, electron backscatter diffraction, microhardness testing, tensile testing, and scanning electron microscopy were used to characterize microstructure and failure behavior. Fine, multi-oriented reconstructed microstructures formed in all weld zones, while a hardness valley developed in the heat-affected zone on the quenched-and-tempered side. As the machine-displayed secondary-friction pressure increased from 1.43 to 2.14 MPa, the actual secondary-friction time decreased from 57.3 to 37.5 s. Under the corresponding high-pressure/short-time condition, heat-affected-zone softening was slightly mitigated and tensile strength increased from 743.37 to 755.78 MPa. Different elongations were observed between the two joint types. All specimens fractured in the softened heat-affected zone on the quenched-and-tempered side and exhibited dimple-dominated fracture surfaces. Under the present tensile-testing conditions, the weld zone was not the fracture-controlling region.

Keywords: 1045 steel; continuous-drive friction welding; secondary friction pressure; quenched-and-tempered condition; heat-affected zone softening

Check for updates

Academic Editor: Hardy Mohrbacher

Received: 10 July 2026
Revised: 31 July 2026
Accepted: 3 August 2026
Published: 5 August 2026

Copyright: © 2026 by the authors. Licensee MDPI, Basel, Switzerland. This article is an open access article distributed under the terms and conditions of the Creative Commons Attribution (CC BY) license.

1. Introduction

Large-diameter rod-like components, such as piston rods used in excavator boom hydraulic cylinders, are critical load-bearing parts in the hydraulic systems of construction machinery. During service, these components are commonly subjected to complex loads, including axial tension–compression, bending, impact and reciprocating friction. The connection region between the rod body and the rod head serves not only as a load-transfer zone, but also as a region sensitive to manufacturing defects, microstructural inhomogeneity and stress concentration. Its joining quality directly affects the load-bearing stability, fatigue life and service safety of hydraulic cylinders. Skowrońska et al. [1] reviewed the materials, heat treatments and surface-modification methods used for hydraulic-actuator components, emphasizing the importance of material selection and surface condition. Dhanya et al. [2]

identified inclusions and surface roughness as important contributors to the failure of a carbon steel piston rod. Ding et al. [3] associated the structural configuration and local stress concentration of a hydraulic-cylinder end cap with fatigue failure. Wang et al. [4] showed that cracking and degradation of the chromium-plated layer impaired the surface integrity of a piston rod. For in-service integrity assessment, Zhang et al. [5] developed a method for detecting longitudinal and transverse cracks in hydraulic-cylinder piston rods. Solazzi and Buffoli [6] evaluated material selection and structural performance from the perspective of fatigue design, while Zhang et al. [7] demonstrated that manufacturing-process optimization could improve the load-bearing safety of a connecting rod. Therefore, developing a stable joining process suitable for large-diameter rod-like components is of great significance for improving the manufacturing quality and service reliability of key components in construction machinery.

Rotary friction welding (RFW) is a category of solid-state joining processes in which frictional heat is generated by the relative rotational motion of one workpiece against another under axial pressure. According to the manner in which rotational energy is supplied, RFW mainly includes continuous-drive friction welding (CDFW) and inertia friction welding (IFW). In CDFW, the rotating workpiece is continuously driven by a motor during the friction stage, generally at a prescribed rotational speed. In contrast, IFW relies on the kinetic energy stored in a flywheel, and the rotational speed decreases continuously after contact as the stored energy is dissipated. The present study employs CDFW, which is particularly suitable for joining shaft- and rod-like components. During CDFW, the interfacial material undergoes plasticization, extrusion and metallurgical bonding under the combined effects of frictional heating and axial pressure. Consequently, solidification defects and coarse solidification microstructures commonly associated with fusion welding can be avoided. Farbakhti et al. [8] reviewed similar and dissimilar rotary friction welding of steels and pointed out that interfacial heat input, plastic flow and microstructural evolution are the key factors governing joint performance. Zhang et al. [9] investigated heat distribution, material flow and microstructural evolution in CDFW joints of 45 steel, showing that heat-input distribution affects flash formation and microstructural variation. Ou et al. [10] reported that friction time changes the heat input, material flow and mechanical properties of CDFW joints; their subsequent study further demonstrated that joint geometry also affects the local thermomechanical process and microstructural evolution [11]. Banerjee et al. [12] indicated that the thermomechanical process in CDFW joints of AISI 8630 low-alloy steel influences the microstructural state and tensile response. Firmanto et al. [13] correlated the microstructural characteristics of rotary-friction-welded carbon steel/stainless steel joints with their tensile strength. Marir et al. [14] evaluated the tensile efficiency and fatigue life of similar and dissimilar carbon steel joints produced by rotary friction welding.

The microstructure and properties of friction-welded steel joints are highly sensitive to process parameters. Belkahla et al. [15] revealed significant relationships among welding parameters, microstructure and mechanical properties in rotary-friction-welded C45/16NiCr6 steel rods. Trung and Nam [16] reported that friction pressure and friction time affected the weld-zone microstructure and hardness of rotary-friction-welded AISI 1030 medium-carbon steel joints. Boumerzoug et al. [17] further showed that rotational speed influenced interfacial mixing, recrystallization behavior, crystallographic characteristics and local microhardness in rotary-friction-welded C45/E335 medium-carbon steel joints. Aoki et al. [18] found that applied pressure altered plastic deformation and local hardening in linear friction-welded martensitic steel joints. These steel-based studies demonstrate that friction pressure, friction duration and rotational speed affect the local thermal and deformation histories of friction-welded joints. In continuous-drive friction

welding, friction pressure can change the interfacial contact condition, material plasticization, axial extrusion behavior and actual friction duration, thereby influencing the local microstructure and properties of the joint.

For large-diameter rotary-friction-welded steel joints, spatial inhomogeneity requires particular attention. Priymak et al. [19] reported that friction force affected phase-transformation behavior, phase composition, microstructural homogeneity, microhardness and impact toughness in 73 mm diameter tubular joints of 32HGMA and 40HN2MA medium-carbon alloy steels. During rotary friction welding, the interfacial linear velocity increases with radius, i.e., $v = \omega r$, providing a geometric basis for radial differences in frictional heat generation and plastic deformation. Liu et al. [20] experimentally and numerically identified an inherent temperature difference between the center and periphery of rotary-friction-welded high-carbon steel joints and showed that insufficient heat input at the interface center could result in unbonded regions. These steel-based findings indicate that large-diameter friction-welded joints should be evaluated not only in terms of overall heat input, but also by considering radial thermomechanical gradients and their effects on local microstructure and properties.

In friction-welded joints, the weld zone (WZ) and thermomechanically affected zone (TMAZ) usually experience high temperature and severe plastic deformation, leading to fragmentation, elongation, rearrangement and grain refinement of the original microstructure. Priymak et al. [21] pointed out that the microstructural evolution in the TMAZ of rotary-friction-welded medium-carbon steel joints is significantly affected by local thermomechanical action. Jin et al. [22] revealed the relationship among shear deformation, dynamic recrystallization and mechanical response near the friction interface through quasi-in-situ observation. Gaikwad et al. [23] also showed that microstructural evolution and hardness variation near the steel-side interface in carbon steel/nickel-based superalloy friction-welded joints are closely related to local thermomechanical action. Therefore, sufficient reconstruction and grain refinement in the WZ are essential for ensuring metallurgical bonding and local load-bearing capacity of friction-welded joints. However, for QT/AR joints composed of quenched-and-tempered 1045 steel and as-rolled 1045 steel, joint performance depends not only on whether the WZ is sufficiently reconstructed, but may also be limited by softening of the heat-affected zone on the quenched-and-tempered side. The QT-side HAZ is mainly affected by the welding thermal cycle and undergoes relatively weak plastic deformation. Its microstructural and hardness variations are closely related to the thermal stability of the quenched-and-tempered microstructure during welding thermal cycling. The reheating response of quenched-and-tempered medium-carbon steels depends strongly on the initial microstructure and tempering conditions. Sun et al. [24] found that tempering temperature altered the microstructure and mechanical properties of induction-quenched 45 steel, while Woźniak et al. [25] showed that high-tempering temperature and holding time affected the hardness and tensile behavior of C45 steel. Tolouei et al. [26] demonstrated that the as-quenched microstructure governed the subsequent tempering response, and Borisov et al. [27] related the property evolution of a Si-rich low-alloy medium-carbon steel to carbide precipitation and retained-austenite decomposition. These findings indicate that the QT-side HAZ is sensitive to microstructural and property changes during the welding thermal cycle. Therefore, when quenched-and-tempered 1045 steel undergoes another welding thermal cycle during CDFW, the QT-side HAZ can easily become a sensitive region for local softening and property degradation.

Based on the above studies, for Ø60 mm large-diameter QT/AR 1045 steel CDFW joints, the key issue is not only whether sufficient metallurgical bonding can be achieved at the welding interface, but also how to balance thermomechanical reconstruction in the WZ with thermal-cycle-induced softening in the QT-side HAZ. On the one hand,

during large-diameter rotary friction welding, the interfacial linear velocity increases with radius, which can readily result in radial inhomogeneity in heat input, plastic flow and hardness distribution. On the other hand, quenched-and-tempered 1045 steel tends to undergo recovery, re-tempering softening and changes in dislocation-related substructures under the welding thermal cycle, making the QT-side HAZ a potential weak region of the joint. Therefore, the performance evaluation of large-diameter QT/AR 1045 steel CDFW joints should focus not only on the degree of WZ reconstruction, but also on the relationship between QT-side HAZ softening and the fracture location. The secondary friction pressure P_1 can change the interfacial contact condition, material plasticization rate and axial extrusion behavior, while also influencing the actual secondary friction time t_1. Therefore, as P_1 increases, the actual t_1 decreases simultaneously. Accordingly, the investigated conditions are interpreted as coupled P_1–t_1 conditions, encompassing low-pressure/long-time and high-pressure/short-time regimes. Meanwhile, the initial quenched-and-tempered condition of the QT side may also change the sensitivity of the HAZ to the welding thermal cycle. However, for Ø60 mm large-diameter QT/AR 1045 steel CDFW joints, targeted understanding is still lacking regarding how the P_1–t_1 matching relationship affects WZ reconstruction, radial hardness distribution and QT-side HAZ softening, as well as how the initial quenched-and-tempered condition of the QT side influences joint ductility and failure behavior. Therefore, Ø60 mm QT/AR 1045 steel CDFW joints were investigated using OM, EBSD, microhardness testing, tensile testing, and fracture-surface SEM characterization to identify the tensile-fracture-controlling region under the investigated welding conditions.

2. Materials and Methods

2.1. Materials and Welding Procedure

QT/AR continuous-drive friction-welded joints were fabricated using 1045 medium-carbon steel rods with a diameter of 60 mm. Two quenched-and-tempered steels and one as-rolled steel were used, designated as QT-A, QT-B and AR, respectively. QT-A and QT-B served as the QT-side base metals, while AR was used as the as-rolled counterpart. During welding, the QT steel was placed on the rotating side and the AR steel on the feeding side. The local elemental compositions of the QT-A, QT-B, and AR base materials were semi-quantitatively analyzed using a GeminiSEM 300 field-emission scanning electron microscope (Carl Zeiss Microscopy GmbH, Jena, Germany) equipped with an EDS system at the center, mid-radius, and near-periphery regions of each rod cross-section. These three radial regions were selected to assess possible radial compositional heterogeneity in the 60 mm diameter rods. The values reported in Table 1 represent the compositional ranges obtained from measurements at these three regions.

Table 1. Chemical compositions of QT-A, QT-B and AR base metals (wt.%).

Steel	C	Si	Mn	P	S	Cr	Mo
1045 Steel (QT-A)	0.42–0.47	0.2–0.25	0.4–0.5	<0.015	<0.02	<0.05	<0.001
1045 Steel (QT-B)	0.42–0.47	0.2–0.25	0.4–0.6	<0.015	<0.02	<0.05	<0.001
1045 Steel (AR)	0.45–0.49	0.27–0.3	1.12–1.23	<0.02	<0.01	<0.2	<0.03

The reported values represent the compositional ranges obtained by SEM-EDS at the center, mid-radius, and near-periphery regions of each rod cross-section.

QT-A and QT-B were subjected to different quenching-and-tempering schedules before welding. The corresponding heat-treatment parameters and measured initial hardness values are summarized in Table 2.

Table 2. Quenching-and-tempering schedules and initial hardness of the QT-A and QT-B base materials.

Steel	Austenitizing Condition	Quenching Medium	Tempering Temperature (°C)	Tempering Time (min)	Cooling After Tempering	Initial Hardness (HV)
QT-A	850 °C/180 min	Water	500	180	Air cooling	250 ± 10
QT-B	840 °C/120 min	Water	530	150	Air cooling	230 ± 10

The welding experiments were conducted using a WF140S-2400 continuous-drive friction welding machine (SAKAE INDUSTRIES Co., Ltd., Yokohama, Japan). Before welding, the specimen end faces were machined and cleaned to ensure stable contact and axial alignment. The CDFW setup and the variations in rotational speed and axial pressure with time are shown in Figure 1a,b, respectively. The welding process consisted of three sequential stages: primary friction, secondary friction, and upsetting. During the primary-friction stage, the machine-displayed hydraulic pressure P_0 was applied for a duration t_0, after which the pressure was increased to the secondary-friction pressure P_1. The machine-displayed hydraulic pressure P_d was converted to the nominal contact pressure p_n according to the following:

$$p_{\mathrm{n}} = (P_{\mathrm{d}} - p_{\mathrm{r}})\frac{A_{\mathrm{c}}}{A_{\mathrm{w}}}, \tag{1}$$

where p_{r} is the sliding-resistance pressure (0.01 MPa), and $\frac{A_{\mathrm{c}}}{A_{\mathrm{w}}} = 28.26$ is the ratio of the main hydraulic-cylinder area to the effective workpiece contact area. Accordingly, the machine-displayed P_1 values of 1.43, 1.96, and 2.14 MPa corresponded to nominal contact pressures of approximately 40, 55, and 60 MPa, respectively. The secondary-friction stage was terminated automatically when the preset axial displacement was reached. Therefore, t_1 was the actual duration recorded from the application of P_1 to the attainment of the preset displacement rather than an independently preset parameter. After rotation stopped, the machine-displayed upsetting pressure P_2 was applied and maintained for a duration t_2.

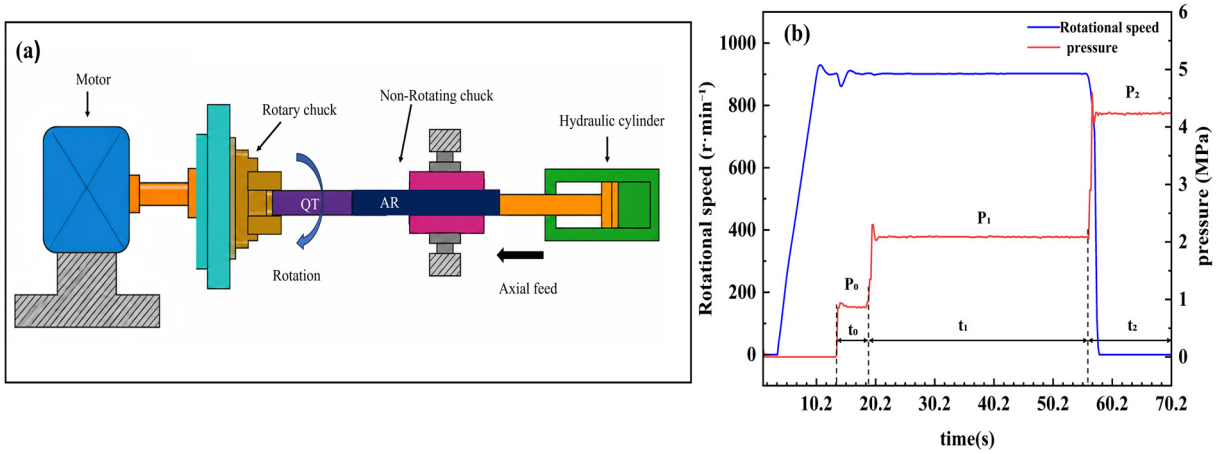


Figure 1. (**a**) Schematic illustration of the continuous-drive friction welding setup; (**b**) variations in rotational speed and axial pressure with time during the CDFW process.

The welding parameters were progressively screened based on industrial practice, the operating capability of the WF140S-2400 welding machine, and preliminary welding trials. Process stability, flash formation, axial shortening, and macroscopic joint formation were used as the evaluation criteria to establish a stable and practically applicable process window. Within this window, the spindle speed, primary-friction parameters, and upsetting parameters were kept constant, while three secondary-friction pressure levels

were deliberately selected to establish representative $P_1 - t_1$ coupling conditions. The resulting welding parameters are listed in Table 3. Specimens 1#–3# were QT-A/AR joints used to evaluate the effect of different $P_1 - t_1$ matching conditions, while specimen 4# was a QT-B/AR joint welded under the same $P_1 - t_1$ and other parameters as specimen 3# to compare the effect of the initial QT condition. Because the actual secondary-friction duration t_1 decreased with increasing machine-displayed P_1, the differences among joints 1#–3# were interpreted in terms of the coupled $P_1 - t_1$ conditions.

Table 3. Continuous-drive friction welding parameters.

Group No.	Joint Type	Spindle Speed (r/min)	P_0 (MPa)	t_0 (s)	P_1 (MPa)	t_1 (s)	P_2 (MPa)	t_2 (s)
1#	QT-A/AR	900	1	5	1.43	57.3	4.28	15
2#	QT-A/AR	900	1	5	1.96	40.5	4.28	15
3#	QT-A/AR	900	1	5	2.14	37.5	4.28	15
4#	QT-B/AR	900	1	5	2.14	37.5	4.28	15

P_0, P_1, and P_2 are hydraulic pressures displayed by the welding machine. The corresponding nominal contact pressures were converted using the relationship given in Section 2.1. t_1 is the actual secondary-friction duration recorded by the welding machine.

2.2. Microstructural Characterization

After welding, longitudinal-section specimens containing the welding interface were sectioned along the joint axis for OM and EBSD characterization. Metallographic specimens were mechanically ground, polished and etched with a 4% nitric acid alcohol solution for approximately 8 s before observation using an ECLIPSE FN1 optical microscope (Nikon, Tokyo, Japan). EBSD specimens were mechanically polished and then electrolytically polished in a methanol–ethanol mixed solution with a volume ratio of 1:3 to reduce the influence of surface stress. EBSD data were acquired using a C-Nano EBSD detector (Oxford Instruments, High Wycombe, UK) mounted on a Gemini SEM 300 field-emission scanning electron microscope (ZEISS).

2.3. Mechanical Property Testing

The sampling positions and dimensions for microhardness and tensile testing are shown in Figure 2. The microhardness distribution on the longitudinal section of the joints was measured using an HV-1000Z Vickers hardness tester (Shanghai Shangcai Testing Machine Co., Ltd., Shanghai, China) with a load of 1 kgf and a dwell time of 15 s. The welding interface was defined as 0 mm, with the negative side corresponding to the QT side and the positive side to the AR side. The spacing between adjacent test points was 0.2 mm near the WZ and TMAZ, 0.5 mm in the transition regions, and 1.0 mm in the HAZ and base-metal regions away from the interface. Room-temperature tensile tests were performed using a UTM5504 electronic universal testing machine (SUNS, Shenzhen Suns Technology Stock Co., Ltd., Shenzhen, China) at a crosshead displacement rate of 2 mm/min in accordance with ASTM E8/E8M-22 [28]. For each group, three tensile specimens were tested. Tensile strength and elongation after fracture are reported as mean ± standard deviation. After tensile testing, the fracture location was recorded, and typical fracture surfaces were observed using a GeminiSEM 300 field-emission scanning electron microscope (ZEISS).

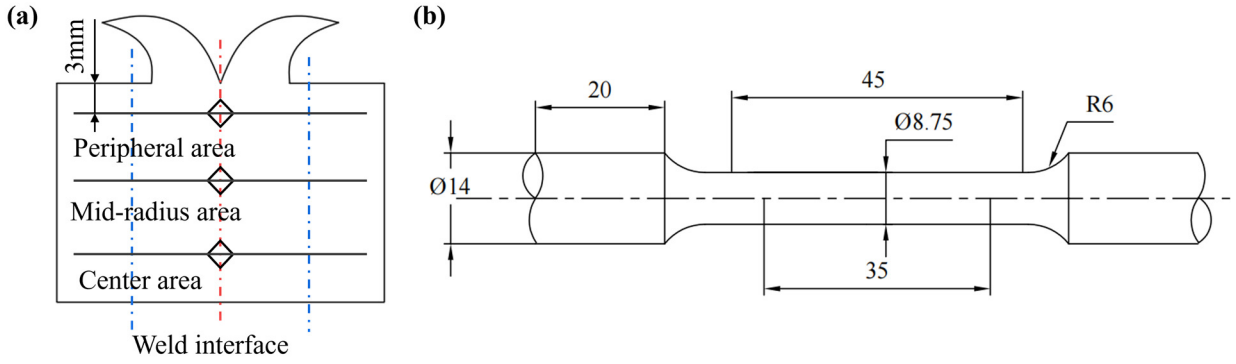


Figure 2. Sampling positions and dimensions for mechanical property testing: (**a**) microhardness paths; (**b**) tensile specimen.

3. Results and Discussion

3.1. Welding Time and Axial Shortening

Figure 3 shows the total welding time and axial shortening of different joints. For the 1#–3# QT-A/AR joints, the spindle speed, primary friction parameters and upsetting parameters were kept constant, while the secondary friction pressure P_1 increased from 1.43 MPa to 2.14 MPa. Correspondingly, the actual secondary friction time t_1 decreased from 57.3 s to 37.5 s, and the total welding time decreased from 77.3 s to 57.5 s. The axial shortening also decreased from 14.4 mm for the 1# joint to 10.7 mm for the 3# joint.

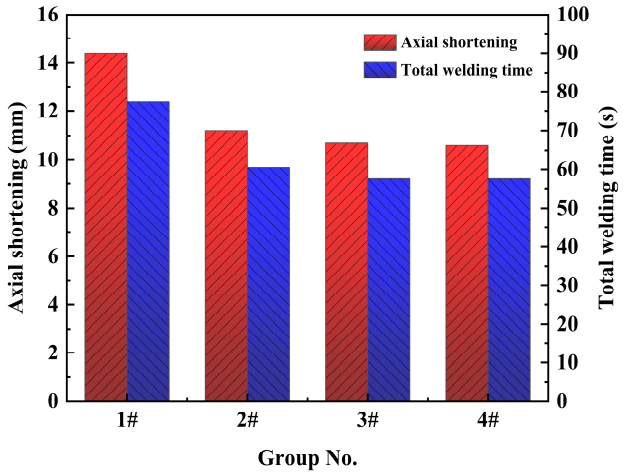


Figure 3. Variations in total welding time and axial shortening of different welded joints.

These results indicate that axial deformation in Ø60 mm large-diameter CDFW joints is not determined by pressure alone, but by the combined effects of pressure level, actual friction duration, material plasticization and axial extrusion. Under the low-P_1/long-t_1 condition, the interfacial material experienced a longer secondary-friction stage and more extensive plasticization and extrusion, resulting in greater axial shortening. In contrast, under the high-P_1/short-t_1 condition, the extrusion duration was reduced, leading to a lower total axial shortening. Therefore, the differences among the 1#–3# joints should be regarded as the result of P_1-regulated pressure–time coupling rather than the independent effect of P_1 alone. This trend is consistent with the finding of Ou et al. [10] that friction duration affects material flow during CDFW. In the present joints, the longer t_1 under the low-P_1 condition promoted more extensive material plasticization and axial extrusion, resulting in greater axial shortening. The 3# and 4# joints exhibited the same total welding time

and similar axial shortening under the same P_1 and t_1 conditions, indicating comparable macroscopic forming behavior for the QT-A/AR and QT-B/AR combinations.

3.2. Microstructural Evolution

3.2.1. Microstructural Evolution Characteristics

Figure 4 shows the initial microstructures of the base metals and the characteristic regions of the 3# joint. The QT-A and QT-B base metals exhibited tempered sorbite (TS), which resulted from the decomposition of the quenched microstructure during high-temperature tempering. The AR base metal consisted mainly of ferrite (F) and pearlite (P), which formed during cooling after hot rolling and exhibited a locally banded morphology. Representative OM observations of the WZ revealed no obvious cracks, interfacial discontinuities or unbonded regions.

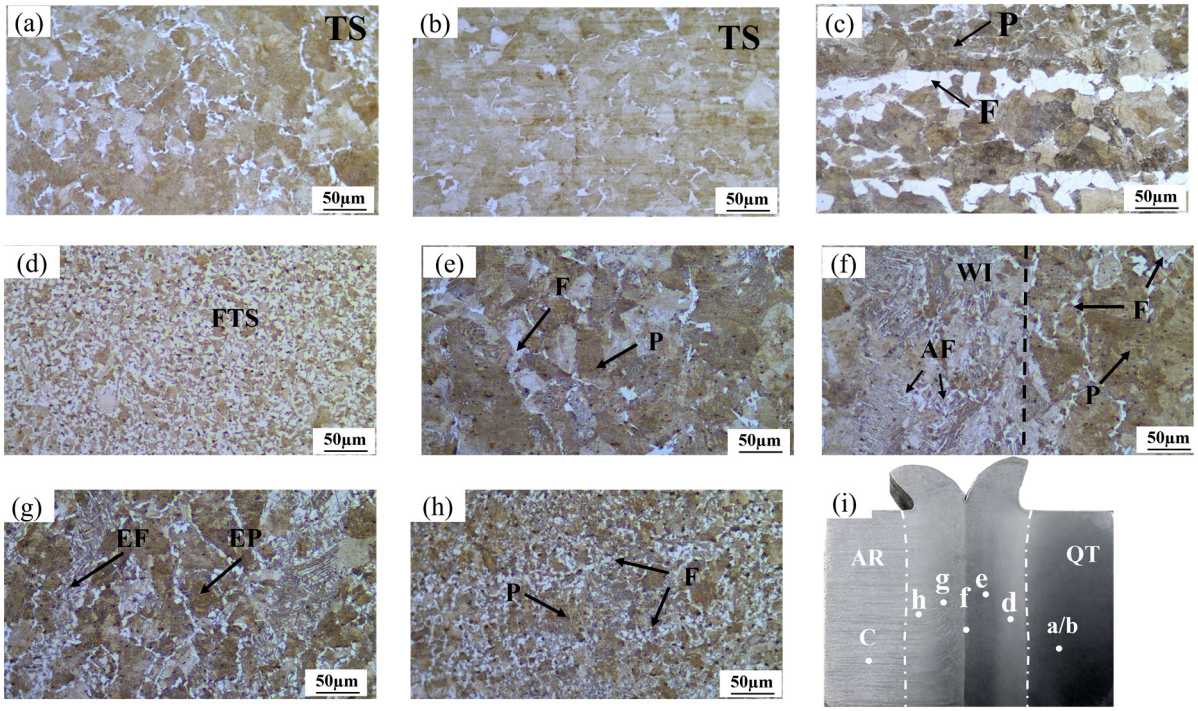


Figure 4. Initial microstructures of the base metals and OM microstructures of characteristic regions in the 3# joint: (**a**) QT-A BM; (**b**) QT-B BM; (**c**) AR BM; (**d**) QT-side HAZ; (**e**) QT-side TMAZ; (**f**) WZ; (**g**) AR-side TMAZ; (**h**) AR-side HAZ; and (**i**) macrograph showing the observation locations. TS, tempered sorbite; FTS, fine tempered-sorbitic morphology; F, ferrite; P, pearlite; AF, acicular ferrite-like morphology; EF, elongated ferrite; EP, elongated pearlite; WI, weld interface.

After welding, distinct axial microstructural gradients developed on the QT and AR sides of the joint. On the QT side, the initial tempered-sorbitic microstructure was retained in the HAZ but became finer and more dispersed under welding reheating, without obvious directional deformation. Closer to the interface, the stronger combined influence of heating and plastic deformation caused the original tempered-sorbitic morphology to become indistinct in the QT-side TMAZ, where ferrite and pearlite were observed. In the WZ, the original tempered-sorbitic morphology largely disappeared under the combined effects of frictional heating and severe plastic deformation, and ferrite and pearlite were observed on the QT side adjacent to the interface. Thus, along the joint axis from the QT base metal toward the interface, the microstructure changed from tempered sorbite, through a reheating-modified fine tempered-sorbitic HAZ and a strongly modified QT-side TMAZ, to the reconstructed WZ.

On the AR side, the initially banded ferrite–pearlite microstructure remained recognizable in the HAZ without pronounced directional elongation. Toward the interface, increasing plastic flow caused ferrite and pearlite to become strongly elongated along the material-flow direction in the TMAZ, forming elongated ferrite (EF) and elongated pearlite (EP). In the WZ, the original banded ferrite–pearlite morphology was extensively disrupted and redistributed under severe thermomechanical action. An acicular-ferrite-like morphology (AF) was observed on the AR side adjacent to the interface, indicating substantial modification of the original ferrite–pearlite morphology under the welding thermomechanical cycle. Accordingly, along the joint axis from the AR base metal toward the interface, the microstructure changed from locally banded ferrite–pearlite, through retained ferrite–pearlite in the HAZ and elongated ferrite–pearlite in the TMAZ, to the reconstructed WZ.

These axial microstructural gradients show that the HAZ was characterized mainly by reheating-induced modification of the initial microstructure, whereas the TMAZ additionally exhibited plastic-flow-related elongation and morphological modification. In the WZ, the original microstructural morphologies were extensively disrupted and reconstructed. These regional characteristics are consistent with the stronger combined thermal and plastic-deformation effects near the friction-welding interface [21].

Figure 5 compares the QT-side HAZ and AR-side TMAZ of the 1#–4# joints. All QT-side HAZs retained a fine and dispersed tempered-sorbitic morphology without obvious plastic-flow features. For the 1#–3# QT-A/AR joints, the dominant constituent type remained unchanged, but differences in the local characteristic scale and spatial distribution were observed. The 1# HAZ exhibited more pronounced local heterogeneity and relatively coarse morphological features, whereas the 3# HAZ showed a finer and more closely distributed morphology than the 1# HAZ.

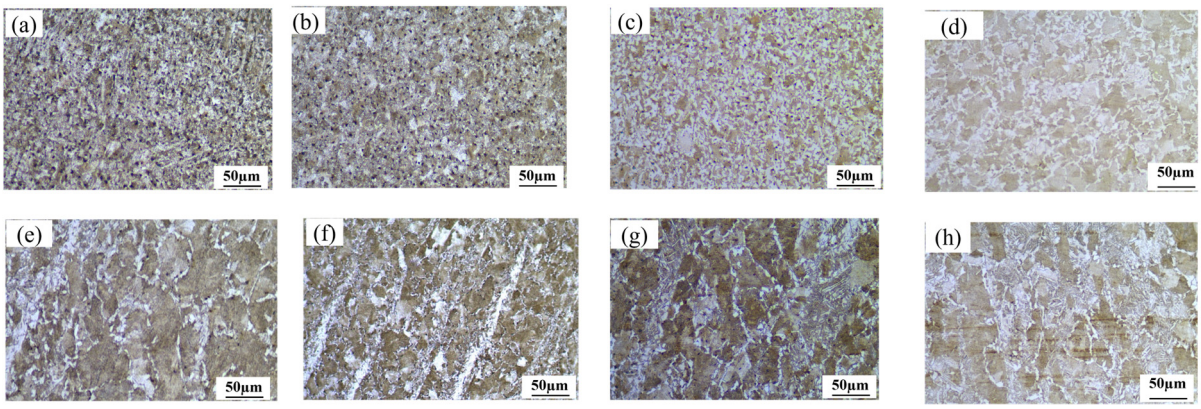


Figure 5. OM microstructures of QT-side HAZ and AR-side TMAZ in different joints: (**a**–**d**) QT-side HAZ; (**e**–**h**) AR-side TMAZ; (**a**,**e**) 1#; (**b**,**f**) 2#; (**c**,**g**) 3#; and (**d**,**h**) 4#.

All AR-side TMAZs contained ferrite and pearlite elongated along the material-flow direction, confirming pronounced plastic flow in this region. In the 1# joint, the elongated constituents appeared relatively broad and continuous. In the 2# joint, the flow-aligned morphology was more pronounced. In the 3# joint, the elongated constituents exhibited more evident local segmentation and reduced continuity. These morphological differences may be associated with the competing effects of pressure level and actual friction duration on material flow. Under the low-P_1/long-t_1 condition, the longer deformation period and greater axial shortening allowed more sustained material flow and extrusion near the interface, resulting in relatively broad and continuous elongated constituents. In contrast, under the high-P_1/short-t_1 condition, the higher instantaneous pressure may have

promoted local plastic deformation and microstructural fragmentation, whereas the shorter duration and smaller axial shortening limited the sustained flow and rearrangement of the elongated constituents. Consequently, more evident local segmentation and reduced continuity were observed in the 3# joint. Therefore, these morphological differences are interpreted as the result of the coupled effects of pressure level, actual friction duration and axial shortening, rather than the independent effect of any single parameter [16,18].

Under the same welding settings, the 3# and 4# joints also exhibited distinct QT-side HAZ morphologies. Compared with the 3# joint, the 4# HAZ contained relatively coarser and more widely separated morphological features, indicating that the initial QT condition influenced the local microstructural response.

3.2.2. EBSD Microstructural Characterization

To quantitatively compare the WZ and QT-side HAZ under different welding conditions, EBSD characterization was performed on the corresponding regions of the 1#–4# joints. The average grain size, LAGB/HAGB fractions and average KAM are summarized in Table 4.

Table 4. EBSD statistical results of the WZ and QT-side HAZ in different joints.

Region	Specimen	Average Grain Size (μm)	LAGBs (%)	HAGBs (%)	Average KAM (°)
WZ	1#	6.64 ± 4.04	57.2	42.8	3.58 ± 2.17
	2#	7.54 ± 5.26	61.6	38.4	2.11 ± 0.87
	3#	7.69 ± 5.46	68.7	31.3	2.26 ± 0.87
	4#	7.69 ± 5.41	66.4	33.6	1.77 ± 0.76
QT-side HAZ	1#	8.14 ± 5.01	67.0	33.0	2.44 ± 0.86
	2#	6.41 ± 2.84	50.7	49.3	2.25 ± 0.88
	3#	5.30 ± 1.81	43.8	56.2	2.18 ± 1.00
	4#	5.41 ± 1.86	44.3	55.7	1.64 ± 0.78

Figure 6a–d show that the WZs of all joints consisted of fine, multi-oriented grains without a dominant preferred orientation. Priymak et al. [29] also used EBSD to characterize crystallographic restructuring in rotary-friction-welded medium-carbon alloy-steel joints. Combined with the OM observations, the fine, multi-oriented grains and the absence of a dominant preferred orientation indicate that the original microstructures were substantially disrupted and reconstructed under the coupled effects of frictional heating and plastic deformation. According to Table 4, the average WZ grain sizes of the 1#–3# QT-A/AR joints were 6.64 ± 4.04, 7.54 ± 5.26 and 7.69 ± 5.46 μm, respectively, while that of the 4# QT-B/AR joint was 7.69 ± 5.41 μm. Thus, all investigated conditions produced fine, multi-oriented reconstructed WZ microstructures, with average grain sizes ranging from 6.64 to 7.69 μm.

Although the general reconstructed morphology was retained in all WZs, their final grain-boundary and KAM characteristics varied with the coupled P_1–t_1 conditions. As shown in Figure 7, for the 1#–3# QT-A/AR joints, the LAGB fraction increased from 57.2% to 61.6% and 68.7%, while the HAGB fraction decreased from 42.8% to 38.4% and 31.3%, respectively. Rui et al. [30] reported correlations between EBSD-derived kernel average misorientation and dislocation-related deformation in low-alloy steels. Accordingly, KAM is used here as an indirect indicator of local lattice distortion and dislocation-related heterogeneity. The corresponding KAM distributions are shown in Figure 8. The average KAM values of the 2# and 3# WZs were 2.11 ± 0.87° and 2.26 ± 0.87°, respectively, both lower than the 3.58 ± 2.17° measured in the 1# WZ.

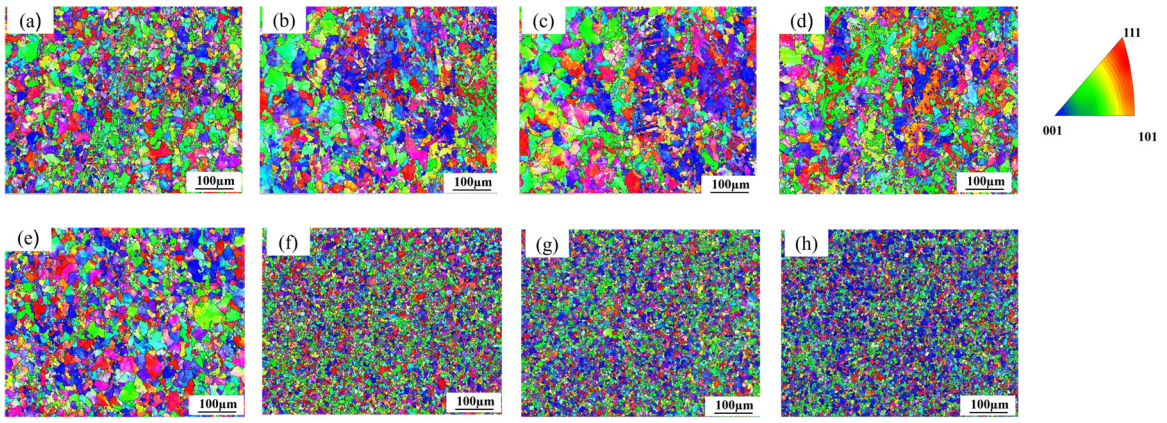


Figure 6. EBSD IPF maps of WZ and QT-side HAZ in different joints: (**a**–**d**) WZ; (**e**–**h**) QT-side HAZ; (**a**,**e**) 1#; (**b**,**f**) 2#; (**c**,**g**) 3#; and (**d**,**h**) 4#.

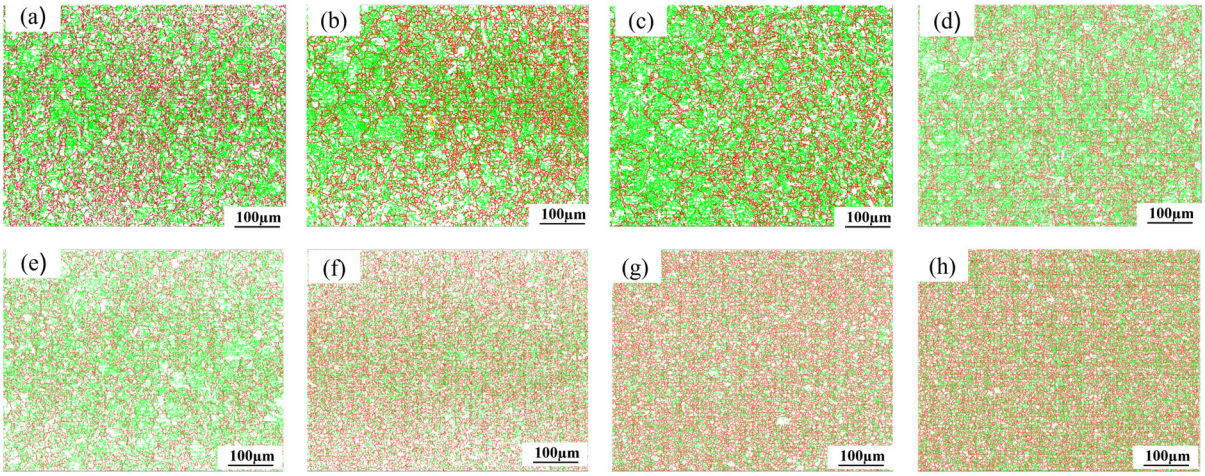


Figure 7. Grain boundary maps of WZ and QT-side HAZ in different joints: (**a**–**d**) WZ; (**e**–**h**) QT-side HAZ; (**a**,**e**) 1#; (**b**,**f**) 2#; (**c**,**g**) 3#; and (**d**,**h**) 4#. Green lines represent low-angle grain boundaries (LAGBs), and red lines represent high-angle grain boundaries (HAGBs).

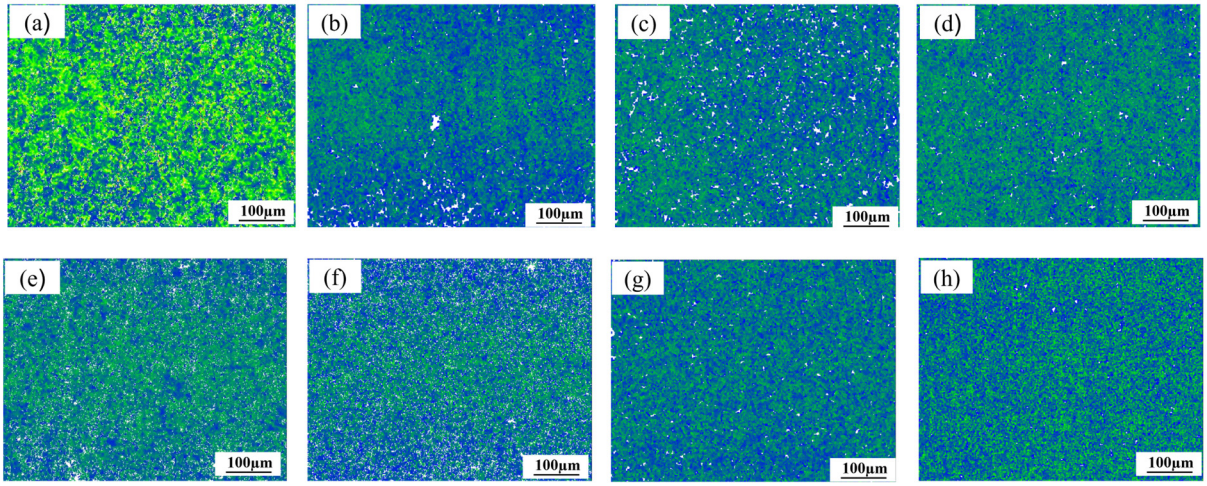


Figure 8. KAM maps of WZ and QT-side HAZ in different joints: (**a**–**d**) WZ; (**e**–**h**) QT-side HAZ; (**a**,**e**) 1#; (**b**,**f**) 2#; (**c**,**g**) 3#; and (**d**,**h**) 4#.

These results define two different final WZ states. The 1# WZ was characterized by a relatively higher HAGB fraction and higher average KAM, whereas the 3# WZ exhibited

an LAGB-dominated boundary network and lower average KAM. This shift coincided with decreases in actual t_1 from 57.3 to 37.5 s and axial shortening from 14.4 to 10.7 mm. The low-P_1/long-t_1 condition therefore corresponded to a longer cumulative interfacial thermomechanical action and an HAGB-richer, higher-KAM final state, while the high-P_1/short-t_1 condition corresponded to an LAGB-dominated, lower-KAM state [10,21].

Compared with the WZ, the QT-side HAZ exhibited a different microstructural response. The OM observations showed that this region retained a fine and dispersed tempered-sorbitic morphology without obvious material-flow features, indicating that its modification was associated mainly with the welding thermal cycle. From the low-P_1/long-t_1 1# condition to the high-P_1/short-t_1 3# condition, the average grain size decreased from 8.14 ± 5.01 to 6.41 ± 2.84 and 5.30 ± 1.81 μm. Concurrently, the LAGB fraction decreased from 67.0% to 50.7% and 43.8%, while the HAGB fraction increased from 33.0% to 49.3% and 56.2%. The average KAM decreased from 2.44 ± 0.86° to 2.25 ± 0.88° and 2.18 ± 1.00°.

The coordinated changes in these EBSD characteristics show a progressive change in the final QT-side HAZ state across the 1#–3# conditions. The 1# HAZ was characterized by a larger average grain size, an LAGB-dominated boundary network and higher average KAM; the 2# HAZ exhibited an intermediate state; and the 3# HAZ showed a smaller average grain size, an HAGB-dominated boundary network and lower average KAM. Because the QT-side HAZ exhibited no pronounced material-flow features, this progression was associated primarily with the change in thermal-cycle duration as the actual t_1 decreased from the low-P_1/long-t_1 to the high-P_1/short-t_1 condition [24,25].

For the 3# and 4# joints welded under the same P_1, t_1 and other welding settings, the WZ grain sizes and LAGB/HAGB fractions were close. The average WZ grain sizes were 7.69 ± 5.46 and 7.69 ± 5.41 μm, and the HAGB fractions were 31.3% and 33.6%, respectively. These similarities indicate that the average WZ grain size and grain-boundary distribution were only slightly affected by the initial QT condition. In the QT-side HAZ, the 3# and 4# joints also exhibited similar average grain sizes and LAGB/HAGB fractions, but the average KAM decreased from 2.18 ± 1.00° in the 3# joint to 1.64 ± 0.78° in the 4# joint. Moreover, the GND distribution of the 4# HAZ shifted toward the lower-density range, as shown in Figure 9. These results show that the initial QT condition had a limited effect on the final grain size and grain-boundary fractions but affected the KAM and retained dislocation-related state of the QT-side HAZ.

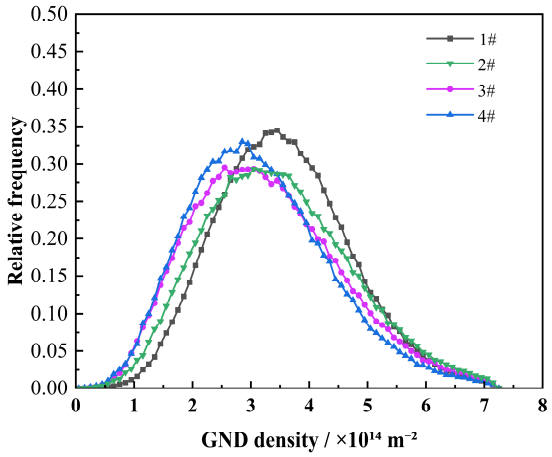


Figure 9. Relative frequency distributions of GND density in the QT-side HAZ of 1#–4# joints.

Taken together, the OM and EBSD results show that all WZs developed fine, multi-oriented reconstructed microstructures, while their grain-boundary and KAM characteristics varied with the coupled P_1–t_1 conditions. The low-P_1/long-t_1 condition corresponded

to a relatively HAGB-richer and higher-KAM WZ state, whereas the high-P_1/short-t_1 condition produced an LAGB-dominated and lower-KAM state. Meanwhile, the QT-side HAZ changed toward a smaller-grained, HAGB-dominated and lower-KAM state, which corresponded mainly to the decrease in actual secondary-friction duration.

3.3. Axial and Radial Microhardness Distribution Characteristics

Figure 10 shows the axial and radial microhardness distributions of the joints, with the welding interface defined as 0 mm. The negative side corresponds to the QT side, and the positive side corresponds to the AR side. As shown in Figure 10a, all 1#–4# joints exhibit an obvious asymmetric hardness distribution. A hardness valley appears in the QT-side HAZ, mainly located approximately −8 to −5 mm from the welding interface. In contrast, a local hardness peak appears within approximately 0–4 mm on the AR side, corresponding mainly to the AR-side TMAZ. This indicates that the QT-side HAZ is the principal softened region, whereas the AR-side TMAZ exhibits local hardening. This asymmetric hardness response corresponds to the observed regional microstructures: the fine near-interface structure and elongated ferrite–pearlite in the AR-side TMAZ are associated with local hardening, whereas the fine tempered-sorbitic morphology in the QT-side HAZ corresponds to the hardness valley. Although elevated temperature generally promotes recovery and thermal softening, the AR-side TMAZ simultaneously undergoes severe plastic deformation and material extrusion under axial pressure during CDFW. The elongated and streamlined ferrite–pearlite morphology shown in Figures 4g and 5e–h indicates intense plastic flow in this region. Such severe deformation may promote the accumulation of deformation-induced lattice defects and dislocations, thereby producing local deformation strengthening. Meanwhile, the finite duration of the thermomechanical cycle, followed by cooling, may limit complete recovery, allowing some deformation-induced defects to be retained. Thus, the local hardness response reflects the competition between thermal softening and deformation strengthening, with deformation strengthening appearing to prevail locally in the AR-side TMAZ. Consequently, deformation-related strengthening may partially offset the thermal-softening effect and contribute to the hardness peak in the AR-side TMAZ. The local hardening observed near the interface is consistent with the finding of Aoki et al. [18] that pressure-induced plastic deformation contributes to local hardening in friction-welded martensitic steel. The pronounced hardness valley on the QT side is associated with reheating and re-tempering of the quenched-and-tempered microstructure, consistent with the hardness reduction in tempered C45 steel reported by Woźniak et al. [25].

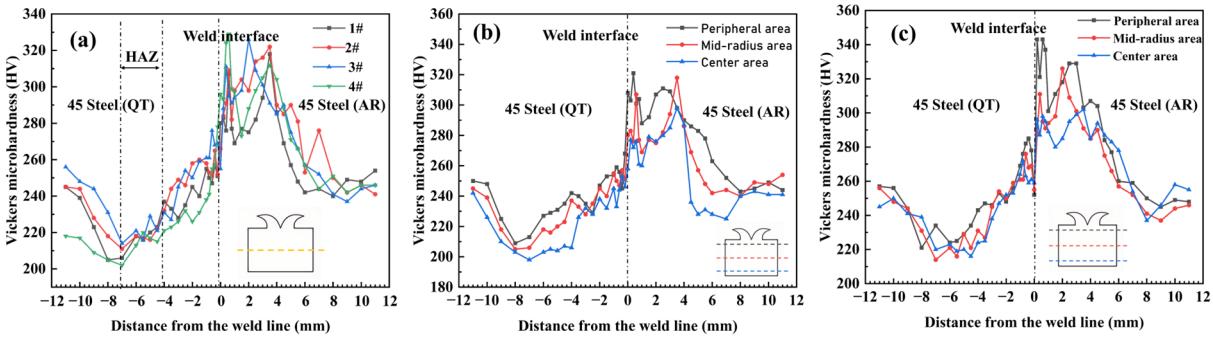


Figure 10. Microhardness distributions of the welded joints: (**a**) axial microhardness profiles of the 1#–4# joints measured at the center; radial-position-dependent axial microhardness profiles of the (**b**) 1# and (**c**) 3# joints.

For the 1#–3# QT-A/AR joints, the minimum hardness of the QT-side HAZ was slightly higher under the high-P_1/short-t_1 condition than under the low-P_1/long-t_1 condition. The

hardness valley of the 1# joint was approximately 210 HV, while those of the 2# and 3# joints were slightly higher. Under the same P_1 = 2.14 MPa and t_1 = 37.5 s conditions, the 3# and 4# joints show similar axial hardness profiles, but differences remain in the QT-side HAZ valley and AR-side TMAZ hardening peak, indicating different HAZ hardness responses in the joints produced with QT-A and QT-B.

Figure 10b,c compare the axial hardness distributions at different radial positions for the 1# and 3# joints, corresponding to the low-P_1/long-t_1 and high-P_1/short-t_1 conditions, respectively. For both joints, the center, mid-radius and near-periphery regions exhibit QT-side HAZ softening and near-interface hardening, indicating that the asymmetric hardness distribution is qualitatively consistent across the three radial positions. In the 1# joint, the maximum near-interface hardness increases from approximately 298 HV at the center to approximately 318 HV at mid-radius and approximately 320 HV near the periphery. In the 3# joint, the corresponding peak increases from approximately 300 HV at the center to approximately 328 HV at mid-radius and approximately 343 HV near the periphery. Therefore, radial hardness inhomogeneity is observed under both welding conditions, while the larger center-to-periphery difference in the 3# joint indicates that this radial variation is more pronounced under the high-P_1/short-t_1 condition. The higher hardness near the periphery may be associated with the greater tangential velocity and correspondingly stronger local thermomechanical action. This result is consistent with the radial thermomechanical inhomogeneity reported by Priymak et al. [19] for large-diameter rotary-friction-welded steel joints.

3.4. Tensile Properties and Macroscopic Failure Behavior

3.4.1. Tensile Properties and Macroscopic Failure Analysis

To evaluate the macroscopic load-bearing capacity of the joints, room-temperature tensile tests were conducted on the QT-A, QT-B and AR base metals and the 1#–4# welded joints. Figure 11 shows the tensile strength, elongation after fracture and macroscopic fracture locations of the joints after tensile testing, and the corresponding results are listed in Table 5. The joint strength retention ratio was calculated according to Equation (2):

$$\eta_{QT} = \frac{R_{m,joint}}{R_{m,QT}} \times 100\% \quad (2)$$

where η_{QT} is the strength retention ratio based on the QT-side base metal, $R_{m,joint}$ is the tensile strength of the joint, and $R_{m,QT}$ is the tensile strength of the QT base metal.

Table 5. Tensile properties of base metals and welded joints.

Material	Tensile Strength (MPa)	Elongation (%)	Strength Retention Based on QT BM (%)	Fracture Location
QT-A BM	823.65 ± 6.36	15.56 ± 0.75	—	—
QT-B BM	810.50 ± 18.31	17.80 ± 0.26	—	—
AR BM	816.01 ± 9.10	17.4 6 ± 0.82	—	—
1#	743.37 ± 10.96	12.10 ± 0.48	90.3	QT-side HAZ
2#	752.7± 7.93	12.02 ± 0.79	91.4	QT-side HAZ
3#	755.78 ± 6.55	12.43 ± 0.95	91.8	QT-side HAZ
4#	748.49 ± 12.68	15.78 ± 1.06	92.34	QT-side HAZ

Tensile strength and elongation after fracture are presented as mean ± standard deviation (n = 3). The strength-retention ratio was calculated using the mean tensile strength of each joint relative to that of the corresponding QT-side base material.

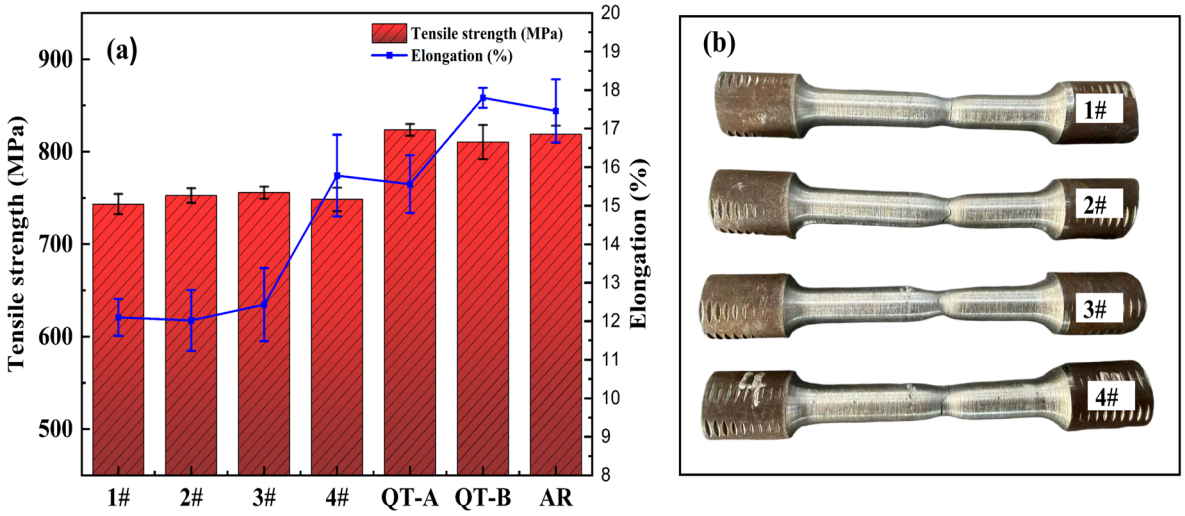


Figure 11. Tensile properties and macroscopic fracture locations of welded joints: (**a**) mean tensile strength and elongation after fracture, with error bars representing standard deviations ($n = 3$); (**b**) macroscopic fracture locations of the 1#–4# joints.

As shown in Figure 11a and Table 5, the tensile strengths of the 1#–4# joints range from 743.37 MPa to 755.78 MPa, lower than those of the corresponding QT-side base metals, with strength retention ratios of 90.3–92.34%. For the 1#–3# QT-A/AR joints, the mean tensile strength increased from 743.37 MPa under the low-P_1/long-t_1 condition to 755.78 MPa under the high-P_1/short-t_1 condition, while the strength retention ratio increased from 90.3% to 91.8%. This modest increase in mean tensile strength occurred concurrently with the slightly higher minimum hardness observed in the QT-side HAZ under the high-pressure/short-time condition, indicating an association between HAZ softening and strength retention.

Under the same P_1 = 2.14 MPa and t_1 = 37.5 s conditions, the tensile strength of the 4# joint is 748.49 MPa, slightly lower than that of the 3# joint. However, its elongation after fracture reaches 15.78%, which is higher than that of the 3# joint, 12.43%, and also higher than those of the 1#–3# joints. Since the strength retention ratio of the 4# joint is calculated based on the QT-B base metal, its value reaches 92.34%, slightly higher than that of the 3# joint. These results show that the two initial QT conditions were associated with different strength-retention and ductility responses. As shown in Figure 11b, all joints fractured in the QT-side HAZ rather than at the welding interface or in the WZ. The fracture locations corresponded to the hardness-valley region in Figure 10a. Therefore, under the present tensile-testing conditions, the WZ was not the fracture-controlling region, and tensile failure localized in the softened QT-side HAZ. The correspondence between the QT-side hardness valley and the tensile fracture location agrees with the microstructure–tensile-property relationship reported by Firmanto et al. [13] for friction-welded steel joints. In addition to local softening, the nonuniform thermal and deformation histories during CDFW may generate a heterogeneous residual-stress field near the weld. Under tensile loading, this residual-stress field may alter the local stress distribution and contribute to the localization of deformation and fracture in the softened QT-side HAZ. Similar near-weld residual-stress characteristics have been reported for rotary-friction-welded steel shafts [31].

3.4.2. Microscopic Fracture Morphology and Fracture Mechanism

To further analyze the fracture mechanism, the tensile fracture surfaces were observed by SEM, as shown in Figure 12. The fracture surfaces exhibited no obvious interfacial separation or large continuous cleavage planes, indicating that interfacial cracking was not the

dominant fracture mechanism. A small number of cleavage-like facets and tearing steps are locally observed in the 1# joint, suggesting relatively inhomogeneous damage propagation in the QT-side HAZ under the low-P_1/long-t_1 condition. In comparison, the 2# and 3# joints show fewer flat regions and more uniform fracture morphologies, indicating improved damage distribution in the softened region under the high-pressure/short-time condition.

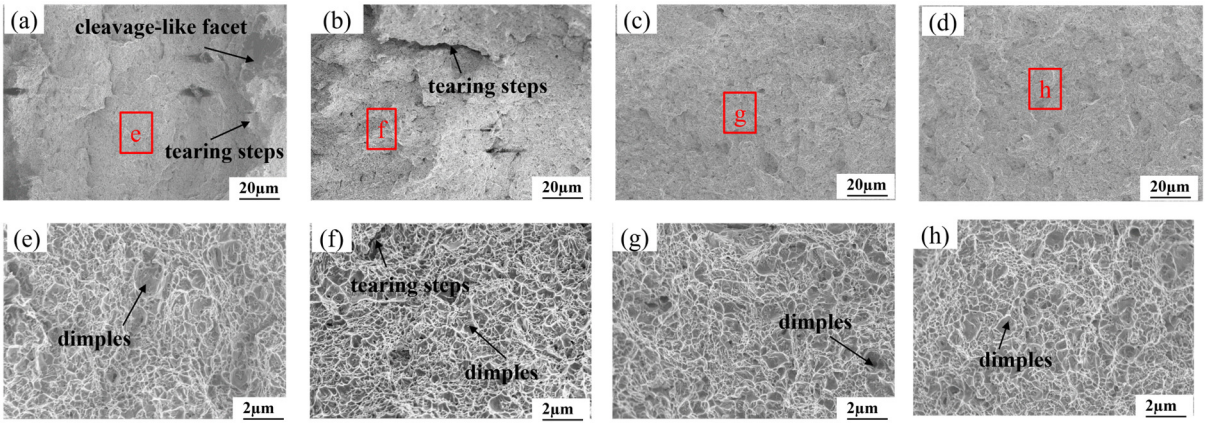


Figure 12. SEM fracture morphologies of tensile specimens fractured in the QT-side HAZ: (**a**–**d**) low-magnification fracture surfaces; (**e**–**h**) high-magnification fracture surfaces; (**a**,**e**) 1#; (**b**,**f**) 2#; (**c**,**g**) 3#; and (**d**,**h**) 4#.

The high-magnification images in Figure 12e–h show that the fracture surfaces of all joints are dominated by dimples, indicating a ductile fracture mode associated with microvoid nucleation, growth and coalescence [32]. Tearing ridges and tearing steps are still locally observed in the 1# and 2# joints, whereas the 3# joint exhibits a more uniform dimple distribution, consistent with its higher strength and reduced QT-side HAZ softening. The 4# joint also shows dimple-dominated fracture with more pronounced plastic features, corresponding to its higher elongation after fracture. These fracture-surface differences are consistent with the higher elongation measured for the QT-B/AR joint and demonstrate different plastic responses between the two joint types.

Although the grain-boundary and KAM characteristics of the WZ varied among the coupled welding conditions, all tensile specimens fractured in the QT-side HAZ at positions corresponding to the hardness valley. Therefore, within the investigated process window, tensile failure was governed primarily by the degree of QT-side HAZ softening rather than by differences in the reconstructed WZ state. The high-P_1/short-t_1 condition corresponded to slightly mitigated QT-side HAZ softening and a higher joint strength. These results suggest that process optimization for large-diameter QT/AR joints should balance adequate WZ reconstruction against excessive thermal exposure and softening of the QT-side HAZ.

4. Conclusions

In this study, Ø60 mm QT/AR 1045 steel joints were fabricated by continuous-drive friction welding. The effects of the P_1–t_1 matching relationship and the initial QT condition on microstructural evolution, HAZ softening and tensile failure behavior were analyzed. The main conclusions are as follows:

(1) As P_1 increased from 1.43 MPa to 2.14 MPa, the actual secondary friction time t_1 of the QT-A/AR joints decreased from 57.3 s to 37.5 s, and the axial shortening decreased from 14.4 mm to 10.7 mm. The differences among the 1#–3# joints reflected the coupled low-P_1/long-t_1 and high-P_1/short-t_1 conditions.

(2) The QT base metals exhibited tempered sorbite, whereas the AR base metal consisted of ferrite and pearlite. After welding, the QT-side HAZ showed a fine tempered-

sorbitic morphology, the WZ exhibited an acicular ferrite-like morphology and fine multi-oriented reconstructed grains, and the AR-side TMAZ contained strongly elongated ferrite and pearlite. The average WZ grain sizes ranged from 6.64 to 7.69 μm, confirming pronounced thermomechanical reconstruction near the interface. As the coupled condition changed from low-P_1/long-t_1 to high-P_1/short-t_1, the WZ changed from a relatively HAGB-richer and higher-KAM state to an LAGB-dominated and lower-KAM state, while the QT-side HAZ changed toward a smaller-grained, HAGB-dominated and lower-KAM state.

(3) The joints exhibited an asymmetric hardness distribution characterized by QT-side HAZ softening and near-interface hardening. The hardness valley was mainly located approximately −8 to −5 mm from the interface on the QT side. Compared with the low-P_1/long-t_1 condition, the high-P_1/short-t_1 condition was associated with a slightly higher minimum hardness in the QT-side HAZ and a higher mean tensile strength, increasing from 743.37 to 755.78 MPa. Radial hardness measurements of the 1# and 3# joints showed that the maximum near-interface hardness increased from the center to the near-periphery under both welding conditions, from approximately 298 to 320 HV for the 1# joint and from approximately 300 to 343 HV for the 3# joint. The radial variation was more pronounced under the high-P_1/short-t_1 condition.

(4) Under the same P_1, t_1, and other welding settings, the QT-B/AR joint exhibited a higher elongation after fracture than the QT-A/AR joint, demonstrating an observed difference in ductility between the two joint types. All specimens fractured in the softened QT-side HAZ and exhibited dimple-dominated fracture surfaces. Under the present tensile-testing conditions, the WZ was not the fracture-controlling region. From an engineering perspective, the present results provide guidance for selecting CDFW parameters for Ø60 mm QT/AR 1045 steel piston-rod assemblies, particularly for controlling QT-side HAZ softening while retaining the fine reconstructed microstructure observed in the WZ.

Author Contributions: Conceptualization, S.C., D.Z., Z.Q. and F.T.; methodology, S.C., D.Z., Z.Q. and G.Z.; software, X.M., D.Z. and M.G.; validation, D.Z., Z.Q., G.Z. and X.M.; formal analysis, D.Z. and X.M.; investigation, D.Z. and G.Z.; resources, S.C. and F.T.; data curation, D.Z. and X.M.; writing—original draft preparation, D.Z.; writing—review and editing, D.Z., G.Z., X.M. and F.T.; visualization, D.Z. and X.M.; supervision, S.C., M.G. and F.T.; project administration, S.C. and M.G.; funding acquisition, S.C. All authors have read and agreed to the published version of the manuscript.

Funding: This study was financially supported by the Bagui Young Top-notch Talents Cultivation Program.

Data Availability Statement: The original contributions presented in this study are included in the article. Further inquiries can be directed to the corresponding author.

Conflicts of Interest: Author Zuojin Qin, Mingqian Gao, and Fuyuan Tian were employed by the company Liugong Machinery Co., Ltd., The remaining authors declare that the research was conducted in the absence of any commercial or financial relationships that could be construed as a potential conflict of interest.

References

1. Skowrońska, J.; Kosucki, A.; Stawiński, Ł. Overview of Materials Used for the Basic Elements of Hydraulic Actuators and Sealing Systems and Their Surfaces Modification Methods. *Materials* **2021**, *14*, 1422. [CrossRef] [PubMed]
2. Dhanya, M.S.; Ranjith, R.; Manwatkar, S.K.; Kumar Gupta, R.; Narayana Murty, S.V.S. Metallurgical Investigation on Failure of Plain Carbon Steel Piston Rod Used in Hydraulic Jack: Role of Inclusions and Surface Roughness. *Eng. Fail. Anal.* **2023**, *150*, 107346. [CrossRef]
3. Ding, S.; Li, G.; Shi, Y.; Ma, J.; Gao, M. Failure Analysis of a Loader Hydraulic Cylinder and Its End Cap Structure Improvement. *Eng. Fail. Anal.* **2023**, *153*, 107597. [CrossRef]

4. Wang, J.; Zhang, Q.; Shen, W.; Liang, Z.; Chang, C.; Yang, L.; Li, J.; Huang, F. Failure Analysis of a Chromium Plating Layer on a Piston Rod Surface and the Study of Ni-Based Composite Coating with Nb Addition by Laser Cladding. *Metals* **2022**, *12*, 1194. [CrossRef]
5. Zhang, J.; Huang, Y.; Tang, J.; Zhou, F.; Kang, Y.; Feng, B. Inspection of Cracks in the Piston Rod of a Hydraulic Cylinder Using Injected Alternating Current-Field Measurement. *Water* **2022**, *14*, 2736. [CrossRef]
6. Solazzi, L.; Buffoli, A. Fatigue Design of Hydraulic Cylinder Made of Composite Material. *Compos. Struct.* **2021**, *277*, 114647. [CrossRef]
7. Zhang, Z.; Jiao, A.; Lv, X.; Ding, H. Study of Failure Analysis and Manufacturing Processes Improvement of Cracking Connecting Rod. *J. Mech. Sci. Technol.* **2022**, *36*, 5445–5453. [CrossRef]
8. Farbakhti, M.; Hosseini, S.R.E.; Mohammadi, S.A.M.; Sadatabhari, S.; Yuan-Ming, H.; Li, R. Similar and Dissimilar Rotary Friction Welding of Steels: A Review of Microstructural Evolution and Mechanical Properties. *J. Mater. Res. Technol.* **2025**, *36*, 8777–8803. [CrossRef]
9. Zhang, W.; Deng, Y.; Zhan, P.; Zeng, J.; Xiao, S.; Xiao, X. Effects of Joint Heat Distribution on Material Flow and Microstructure in Continuous Drive Friction Welding of 45# Steel. *Proc. Inst. Mech. Eng. Part C J. Mech. Eng. Sci.* **2022**, *236*, 6635–6651. [CrossRef]
10. Ou, Y.; Deng, Y.; Zhang, W.; Zhao, Y.; Zeng, J. Effect of Friction Time on Heat Distribution, Material Flow, and Microstructure of Friction Welding of Dissimilar Steels. *Proc. Inst. Mech. Eng. Part L J. Mater. Des. Appl.* **2023**, *237*, 437–450. [CrossRef]
11. Ou, Y.; Deng, Y.; Zhao, Y.; Zeng, J.; Xiao, S. Mechanical Properties and Microstructure of Conical Joints for Dissimilar Steels Continuous Drive Friction Welding. *J. Mater. Eng. Perform.* **2023**, *32*, 5239–5248. [CrossRef]
12. Banerjee, A.; Ntovas, M.; Silva, L.D.; O'Neill, R.; Rahimi, S. Continuous Drive Friction Welding of AISI 8630 Low-Alloy Steel: Experimental Investigations on Microstructure Evolution and Mechanical Properties. *J. Manuf. Sci. Eng.* **2022**, *144*, 071001. [CrossRef]
13. Firmanto, H.; Candra, S.; Hadiyat, M.A.; Triastomo, Y.P.; Wirawan, I. Tensile Strength and Microstructure of Rotary Friction-Welded Carbon Steel and Stainless Steel Joints. *J. Manuf. Mater. Process.* **2023**, *7*, 7. [CrossRef]
14. Marir, M.A.; Sheng, E.L.; Bachi, I.O.; Isa, M.R. Tensile Efficiency and Fatigue Life of Similar and Dissimilar Carbon Steel Joints Subjected to Rotary Friction Welding. *J. Adv. Join. Process.* **2023**, *8*, 100168. [CrossRef]
15. Belkahla, Y.; Mazouzi, A.; Lebouachera, S.E.I.; Hassan, A.J.; Fides, M.; Hvizdoš, P.; Cheniti, B.; Miroud, D. Rotary Friction Welded C45 to 16NiCr6 Steel Rods: Statistical Optimization Coupled to Mechanical and Microstructure Approaches. *Int. J. Adv. Manuf. Technol.* **2021**, *116*, 2285–2298. [CrossRef]
16. Trung, P.Q.; Nam, P.B.H. Experimental Research on the Effect of the Rotary Friction Welding Process on Carbon Steel AISI 1030. *Key Eng. Mater.* **2022**, *936*, 49–54. [CrossRef]
17. Boumerzoug, Z.; Helal, Y.; Muñoz Bolaños, J.A.; Cabrera Marrero, J.M.; Elhadj, R.; Ayad, A.; Cheniti, B. Microstructural and Mechanical Assessment of a Weld Seam between Two Medium Carbon Steels Using the Rotary Friction Welding Process. *Int. J. Adv. Manuf. Technol.* **2026**, *144*, 6401–6419. [CrossRef]
18. Aoki, Y.; Ushioda, K.; Fujii, H. Effect of Applied Pressure on Microstructure and Hardness of Linear Friction Welded Martensitic Steel. *ISIJ Int.* **2024**, *64*, 372–380. [CrossRef]
19. Priymak, E.Y.; Atamashkin, A.S.; Yakovleva, I.L.; Fot, A.P. Interrelation between the Microstructure and Impact Toughness of the Interface of Welded Joints of 32HGMA and 40HN2MA Steels Produced by Rotary Friction Welding. *Front. Mater. Technol.* **2025**, *2*, 73–85. [CrossRef]
20. Liu, H.; Chen, K.; Wu, Z.; Li, Y.; Morisada, Y.; Fujii, H. A Novel Multi-Stage Pressuring Strategy to Fabricate Sound High-Carbon Steel Joints in Rotary Friction Welding. *J. Manuf. Process.* **2025**, *133*, 957–968. [CrossRef]
21. Priymak, E.Y.; Yakovlev, I.L.; Atamashkin, A.S.; Stepanchukova, A.V. Evolution of Microstructure in the Thermomechanically Affected Zone of Welded Joints of Medium-Carbon Steels in the Process of Rotary Friction Welding. *Met. Sci. Heat Treat.* **2021**, *62*, 731–737. [CrossRef]
22. Jin, F.; Fu, B.; Shen, J.; Li, J.; Li, W.; dos Santos, J.F.; Klusemann, B. Quasi-in-Situ Observation of Microstructure at the Friction Interface: Shear Deformation, Dynamic Recrystallization and Mechanical Responses during Friction Welding Process. *Mater. Charact.* **2023**, *200*, 112911. [CrossRef]
23. Gaikwad, V.T.; Mishra, M.K.; Hiwarkar, V.D.; Singh, R.K.P. Microstructure and Mechanical Properties of Friction Welded Carbon Steel (EN24) and Nickel-Based Superalloy (IN718). *Int. J. Miner. Metall. Mater.* **2021**, *28*, 111–119. [CrossRef]
24. Sun, Y.; He, L.; Gao, Y.; Fang, S.; Li, Z.; Li, H. Effect of Induction Quenching and Tempering Temperature on the Mechanical Properties and Microstructure Evolution of 45 Steel for Linear Guide. *J. Mater. Eng. Perform.* **2024**, *33*, 12312–12321. [CrossRef]
25. Woźniak, W.; Sąsiadek, M.; Jachowicz, T.; Edl, M.; Zając, P. Studies on the Mechanical Properties of C45 Steel with Martensitic Structure after a High Tempering Process. *Adv. Sci. Technol. Res. J.* **2022**, *16*, 306–315. [CrossRef]
26. Tolouei, E.; Hurel, V.; Loucif, A.; Morin, J.-B.; Jahazi, M. Influence of the As-Quenched State and Tempering Temperature on the Final Microstructure and Hardness of a High Strength Medium Carbon Steel. *Mater. Chem. Phys.* **2024**, *325*, 129765. [CrossRef]

27. Borisov, S.; Borisova, Y.; Tkachev, E.; Kniaziuk, T.; Kaibyshev, R. Tempering Behavior of a Si-Rich Low-Alloy Medium-Carbon Steel. *Metals* **2023**, *13*, 1403. [CrossRef]
28. *ASTM E8/E8M-22*; Standard Test Methods for Tension Testing of Metallic Materials. ASTM International: West Conshohocken, PA, USA, 2022. [CrossRef]
29. Priymak, E.Y.; Lobanov, M.L.; Belikov, S.V.; Karabanalov, M.S.; Yakovleva, I.L. Structure Formation Patterns and Crystallographic Texture in Welded Joints of Medium-Carbon Alloy Steels in the Process of Rotary Friction Welding. *Phys. Met. Metallogr.* **2022**, *123*, 559–566. [CrossRef]
30. Rui, S.-S.; Han, Q.-N.; Wang, X.; Li, S.; Ma, X.; Su, Y.; Cai, Z.; Du, D.; Shi, H.-J. Correlations between Two EBSD-Based Metrics Kernel Average Misorientation and Image Quality on Indicating Dislocations of Near-Failure Low Alloy Steels Induced by Tensile and Cyclic Deformations. *Mater. Today Commun.* **2021**, *27*, 102445. [CrossRef]
31. Uhlenberg, L.; Baumgartner, J.; Rößler, C.; Schmicker, D.; Köhler, M.; Trommer, F.; Dilger, K. Fatigue Strength Assessment of Friction Welds under Consideration of Residual Stress. *Materials* **2024**, *17*, 3130. [CrossRef] [PubMed]
32. Wciślik, W.; Lipiec, S. Void-Induced Ductile Fracture of Metals: Experimental Observations. *Materials* **2022**, *15*, 6473. [CrossRef] [PubMed]

Disclaimer/Publisher's Note: The statements, opinions and data contained in all publications are solely those of the individual author(s) and contributor(s) and not of MDPI and/or the editor(s). MDPI and/or the editor(s) disclaim responsibility for any injury to people or property resulting from any ideas, methods, instructions or products referred to in the content.